AIAA 92-2725
An Investigation of Passive Control Methods for Shock-Induced Separation at Hypersonic Speed

R. Rallo, M. Walsh
NASA-LaRC, Hampton, VA.
Bram van Leer
The University of Michigan, Ann Arbor MI.

AIAA 10th Applied Aerodynamics Conference

June 22-24, 1992 / Palo Alto, CA.

AN INVESTIGATION OF PASSIVE CONTROL METHODS FOR SHOCK-INDUCED SEPARATION AT HYPERSONIC SPEEDS

R. Rallo*, M. Walsh†

NASA Langley Research Center

and

Bram van Leer‡

University of Michigan

Abstract

An investigation into the effectiveness of passive control techniques on shock-induced boundary-layer separation at hypersonic speeds has been conducted. Two approaches to alleviating the turbulent separation losses were examined: (1) porous surface mass transfer and (2) surface grooving. A total of four perforated surfaces with varying porosities were evaluated. Three groove orientations with respect to the free-stream direction were also studied: transverse, swept, and longitudinal. Test results from these passive control techniques were compared to results from an "uncontrolled" shock impingement to determine the relative effectiveness of the devices. These comparisons indicated that the porous surface with the greatest porosity provided the largest reduction in the pressure rise across the oblique shock wave; however, the length of the interaction region was significantly extended. Each of the grooved configurations examined increased the peak pressure value. In general, the grooved surfaces tested were found to be an ineffective means of suppressing the losses across the shock system at hypersonic (M=6) speeds.

In addition to the experimental efforts to examine the shock-induced boundary-layer separation, two-dimensional, thin-layer Navier-Stokes computations were undertaken. Results from the Navier-Stokes code compared favorably with the experimental data for the solid wall (i.e. reference) configuration.

Nomenclature

a	groove depth
b	groove width
C_p	pressure coefficient
FV	finite volume
k	thermal conductivity constant
k_{BL}	Baldwin-Lomax coefficient
M	Mach number
n	wall-normal direction
P	pressure
P_r	Prandtl number
q	heat flux
R_e	free-stream Reynolds number

* Aerospace Engineer, Member AIAA, Experimental Flow Physics Branch

† Aerospace Engineer, Assistant Head, Experimental Flow Physics Branch

‡ Professor Aerospace Department, Senior Member AIAA

R_{el}	Reynolds number per unit length
t	rib thickness
T	temperature
U	streamwise velocity
V	wall-normal velocity
X_L	streamwise flat-plate length
Y_L	flat-plate semispan
X/X_L	non-dimensionalized streamwise length
Y/Y_L	non-dimensionalized spanwise length
x,y,z	Cartesian coordinates

Greek Symbols

β	flow-deflection angle
δ	boundary-layer thickness
θ	shock-wave angle
μ	viscosity coefficient

Subscripts

e	effective
o	stagnation conditions
t	turbulence quantities
w	wall conditions
∞	freestream conditions

Introduction

Considerable attention has been directed toward controlling shock-induced boundary-layer separation at hypersonic speeds. This interest stems, in part, from the current efforts to develop a single-stage-to-orbit hypersonic vehicle. During transatmospheric flight, shock waves generated by a lifting body, a deflected control surface, or a wingbody juncture can separate the boundary layer adversely affecting a vehicle's lift and drag characteristics. The problem of shock-wave-induced separation is also relevant at the inlet of a supersonic combustion ramjet (scramjet) engine, where reflected compression and expansion waves interact with the boundary layer on the opposing wall. These interactions can significantly increase the pressure loads and heat transfer rates at the surface of the inlet. Bogdonoff and Poddar[1] noted that such interactions "are of fundamental interest to the efficient design of high-speed inlets where the losses, exit flow details, and character of the flow, are of key importance in ... combustor design."

Therefore, the behavior of a compressible, turbulent boundary layer in the presence of an incident shock is of particular interest. It is known from compressible flow theory that an oblique shock slows the velocity of incoming fluid, and that this deceleration is accompanied by a steep rise in pressure. As the shock strength is increased, the boundary layer separates[2]. If the near wall momentum is augmented or the pressure differential across the shock decreased, separation may be suppressed.

Efforts to suppress or eliminate shock-induced separation can be divided into two categories: active control systems (e.g. suction, injection, or wall-cooling) and passive control systems (e.g. porous wall mass transfer, vortex generators, surface grooving). The majority of this research, summarized in Reference [3], has been conducted at supersonic and transonic speeds.

Active control systems affect changes in the boundary layer through either mass addition or mass removal at the surface. The power required for this surface mass transfer may be significant and result in a net degradation in the vehicle's performance. Bertelrud [4] stated that while active suction and/or injection "may give a gross drag reduction, the energy required for pumping may preclude a net gain." This fact combined with the added weight and mechanical complexity of the active control system suggests the need for

alternatives.

Therefore, the study discussed herein will focus on two passive control techniques in the presence of a high-speed, high Reynolds number shock/boundary-layer interaction. The passive control methods to be examined are:

(1) a reduction of the adverse pressure gradient through perforated/porous surfaces, and

(2) the modification of near-wall momentum distribution through surface grooving.

Previous Experimental Work

At low speeds, passive control through porous mass transfer has been proven to be a viable means of controlling boundary-layer separation[5, 6, 7]. One of the most common applications of porous surface mass transfer for passive drag reduction occurs in supercritical airfoil design. In the vicinity of a terminating normal shock a portion of the upper surface of the airfoil is replaced by a thin perforated sheet covering a small cavity located in the surface. The slower, high pressure air behind the shock is bled through the cavity to the low pressure region in front of the shock. This substantially thickens the upstream boundary layer creating compression waves which weaken the incident shock. The total pressure loss through the shock system is, therefore, reduced by creating a smoother, more isentropic compression[8]. In addition, the pressure rise is spread over a greater streamwise distance which helps to reduce the velocity and temperature gradients near the surface.

Work completed by Nagamatsu et al.[6] achieved sizable drag reductions for a transonic airfoil with porous surface modifications. Tests were performed on a 14% thick NASA supercritical airfoil with a maximum porosity of 10.4%, based on the ratio of the open area divided by the total area of the perforated surface. Nagamatsu obtained drag reductions of up to 40% at a Mach number of 0.83.

More recently, Bauer and Hernandez [7] investigated the effectiveness of using porosity to minimize crossflow shock/boundary-layer separation at supersonic speeds. Results obtained for a solid surface swept-conical-wing configuration at a Mach number of 1.70 were compared to results with a porous surface. For a porosity of 22% the researchers noted a decrease in the shock strength and negligible amounts of separated flow. It was further determined that an airfoil with 22% porosity more effectively reduced the shock strength than an airfoil with 11% porosity.

Surface grooving, the second passive control technique investigated in the present tests , was first introduced during the 1960's as a means of controlling or delaying separation in diffusers[9, 10]. More recently, surface grooving has been shown by Howard et al. [11] to significantly reduce the drag on bluff bodies at subsonic speeds. Since bluff body drag is typically dominated by afterbody flow separation effects[12], a series of circumferential (transverse) grooves were machined into the aft section of an axisymmetric model. The optimal positioning and sizing of the grooves resulted in significant drag reductions, in some instances up to 50%.

The effectiveness of surface grooving may be attributed to several factors: (1) the grooves shed vorticity which energize the boundary layer, (2) they act as a laminar boundary-layer trip mechanism, and (3) they perform a function similar to a "roller bearing"[9]; that is, the grooves break up the larger separated flow region into smaller separated regions effectively creating a slip condition at the wall[13]. A modification of the "no-slip" boundary condition significantly reduces the distance to reattachment and decreases the drag.

The objective of the this investigation is to determine whether the passive separation control benefits demonstrated at low speeds can be obtained at hypersonic Mach numbers.

Experimental Methods

The Wind Tunnel

The NASA Langley Mach 6 High Reynolds Number Wind Tunnel (Figure 1) is used to study turbulent

boundary layers and free-mixing shear layers over a wide range of Reynolds numbers. The blowdown facility uses air as its test medium and operates at Reynolds numbers varying between 0.8×10^6 and 37×10^6 per foot. Maximum stagnation pressures of 2700 psi at a stagnation temperature of 550^0F are obtainable. The circular tunnel test section is 42 inches long and 12 inches in diameter. High pressure air is supplied upstream of the test section and exhausts downstream into a 41-foot vacuum sphere. At low stagnation pressures (P_0=200 psia), the run time is approximately two minutes and is limited by the volume of the vacuum sphere. The tunnel is vented to atmosphere for higher stagnation pressures ($P_0 \geq 700$ psia) and the run time is dependent on the air supply. For stagnation pressures of 700–1000 psia the run time is essentially unlimited. A more extensive description of the facility and its capabilities may be found in Reference[14].

The Wind Tunnel Model

To investigate passive separation control techniques, a variable geometry two-dimensional model was constructed. The model consisted of a wedge-type shock generator placed above a flat plate, as shown in Figure 2.

The flat-plate model was 36 inches long and 7.75 inches wide. A rectangular cavity (5 X 8.5 X 0.25") in the plate was located 18 inches downstream from the flat-plate leading edge. Interchangeable passive control insert plates were installed into the cavity and tested.

The wedge-type shock generator was 8 inches long and had a span of 5 inches. The spanwise length of the shock generator was limited due to tunnel blockage effects. The shock generator had a sharp leading edge with an included angle of approximately 14.5 degrees. Both the height of the shock generator and its angle of inclination relative to the free stream were variable.

Three types of stainless steel insert plates were examined; porous plates, grooved plates and a baseline solid plate. A total of four perforated surfaces with porosities ranging from 22% open to 28% open, based on the total open area divided by the area of the perforated sheet, were evaluated. The maximum perforated surface thickness was approximately 0.04 inches. The porous plates were mounted to a rectangular support structure using high temperature silicone sealant. Three groove orientations with respect to the free stream were also studied; longitudinal, transverse, and swept (see Figure 3). The effects of a 0.1 inch and a 0.05 inch spacing between the grooves were evaluated. A solid insert plate was also manufactured to obtain "baseline" flat-plate measurements for comparison.

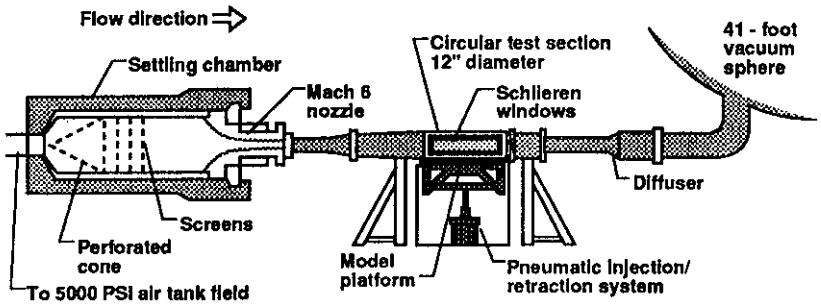

Figure 1 Schematic of the Mach 6 High Reynolds Number Tunnel.

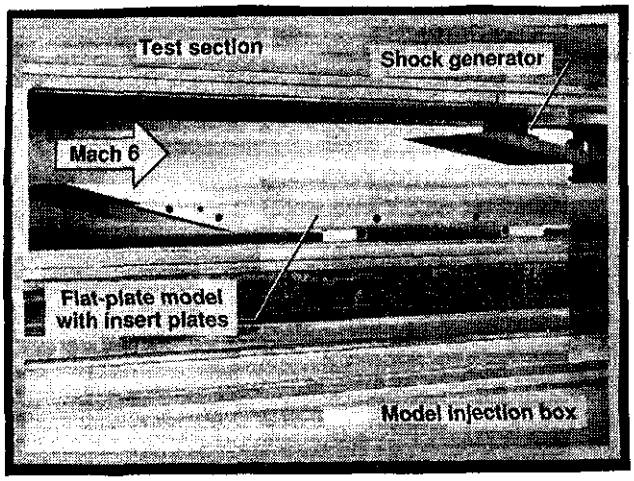

Figure 2 Shock/boundary-layer interaction model in the M6HRN test section.

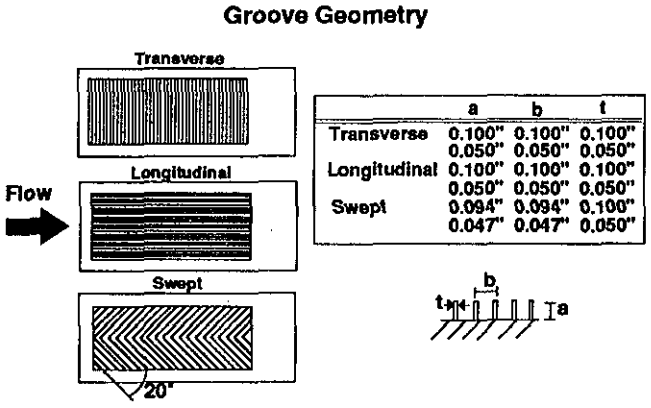

Figure 3 Schematic of grooved boundary-layer control devices.

Numerical Investigations

In addition to the experimental study, computations were performed for the two-dimensional shock/boundary-layer interaction.

Computational Algorithm

The Computational Fluids Laboratory code was developed, by J. Thomas at NASA Langley Research Center, to solve the steady state thin-layer Navier-Stokes equations. The thin-layer Navier-Stokes approximation is obtained by neglecting terms on the order of $\frac{1}{\sqrt{Re_l}}$ and smaller. Therefore, viscous terms with derivatives parallel to the surface of a body are not retained since they are substantially smaller than viscous terms with derivatives normal to the surface. This approximation is especially suited to high-Reynolds number flows where the effects of viscosity are concentrated near surface boundaries.

The thin-layer Navier-Stokes equations are converted to a system of algebraic equations using a semi-discrete finite-volume (FV) method[15]. A spatially split approximate factorization scheme is used to advance the solution in time[16]. Upwind flux-differencing[17] is used to discretize the convective and pressure (inviscid) terms whereas central differencing is used to discretize the diffusive (viscous) terms. The resulting steady-state solution is second-order accurate and independent of the time step.

Initial and Boundary Conditions

The accuracy of the numerical algorithm depends largely on the appropriate selection of initial and boundary conditions. Typically, the conditions specified reflect physical observations and proven computational results. For the shock/boundary-layer interaction problem considered here, free-stream initial conditions are imposed throughout the computational domain. Along the flat plate, no-slip adiabatic wall boundary condi-

tions are applied

$$U_{wall} = tangential\ velocity = 0$$
$$V_{wall} = normal\ velocity = 0$$
$$-k\left(\frac{\partial T}{\partial n}\right) = q_{wall} = heat\ flux = 0$$

The pressure boundary at the solid wall is specified by setting the normal pressure gradient $\left(\frac{\partial P}{\partial n}\right)$ equal to zero. The conditions at the top of the domain are specified using oblique shock jump relations requiring conservation of mass, momentum, and energy. At the entrance of the computational domain, free-stream conditions are imposed on the cell enters located upstream of the impinging shock, and shock jump relations are imposed on the cell centers located downstream of the impinging shock. The boundary conditions at the downstream limit of the computational domain are extrapolated from conditions just inside the domain.

Turbulence Modeling

The time-averaged (or Reynolds-averaged) Navier-Stokes equations are used in conjunction with the Baldwin-Lomax (B-L) mixing-length model to simulate the effects of turbulence. The primary advantage of the B-L turbulence model is that the thickness of the boundary layer need not be specified to close the system of equations. The vorticity distribution is used to determine the relevant length scales. Since the boundary-layer thickness is often difficult to compute, especially for separated flows, the B-L model removes a source of potential error from the Navier-Stokes solutions. Details of the turbulent closure model employed are discussed below.

The Baldwin-Lomax model simulates the effects of turbulence by the introduction of two turbulence modeling parameters —an eddy viscosity coefficient, μ_t, and a turbulent conductivity term, $\frac{\mu_t}{P_{rt}}$. These modeling parameters are related to the laminar flow coefficients by,

$$\mu_e = \mu + \mu_t$$
$$\frac{k_{BL}}{C_p} = \frac{\mu}{P_r} + \frac{\mu_t}{P_{rt}}$$

where μ is the molecular coefficient of viscosity and $\frac{\mu}{P_r}$ is the laminar heat flux. The constant appearing in the above equation is assigned the value, $k_{BL} = 0.4$.

The shear layer is separated into two modeling regions, with dissimilar eddy viscosity coefficients. The turbulence model for the inner region is patterned after the Cebeci-Smith [18] two-layer model. The turbulence model for the outer region is defined such that the location of the boundary-layer edge need not be determined, simplifying the required number of calculations. Additional information regarding the formulation of the B-L turbulence model may be found in Reference[19].

Results and Discussion

Experimental Results

The primary objective of this investigation was to determine whether passive control techniques offer a viable means of minimizing shock-induced boundary-layer separation at hypersonic speeds. With this goal in mind, the first phase of the investigation focused on the behavior of a shock/boundary-layer interaction over a solid surface. Surface pressure measurements, oil flows, and schlieren photography were used to identify basic features of the shock structure at a flow deflection angle of 12.5 degrees. Unless otherwise noted, all of the results presented herein were obtained at the following operating conditions; i.e., P_o=1000 psia, T_o=475 ^{0}F, Re/ft=15.175X10^6, and β=12.5^0. The second phase of the investigation addressed the two passive control techniques previously discussed;

(1) a weakening of the adverse pressure gradient through passive surface perforation,

(2) the modification of near-wall momentum distribution through surface grooving.

Test results from these passive devices were compared to the "uncontrolled" shock impingements to determine their relative effectiveness (See Table 1).

Case	Instrumented Insert Plate	Shock Generator/Flow Deflection Angle β
1	Solid Insert	N/A
2	Solid Insert	β=7.5°,10.0°,12.5°
3	Grooved Insert Longitudinal Narrow & Wide Spacing	β=7.5°,10.0°,12.5°
4	Grooved Insert Transverse Narrow & Wide Spacing	β=7.5°,10.0°,12.5°
5	Grooved Insert Swept Narrow & Wide Spacing	β=7.5°,10.0°,12.5°
6	Porous Insert 28%	β=7.5°,10.0°,12.5°
7	Porous Insert 27%	β=7.5°,10.0°,12.5°
8	Porous Insert 23%	β=7.5°,10.0°,12.5°
9	Porous Insert 22%	β=7.5°,10.0°,12.5°

Table 1 Experimental Test Matrix

This initial discussion of the experimental data is followed by computational results from the two-dimensional Navier-Stokes code (CFL2D). Comparisons between the experimental and computational data are made where possible.

Shock-Induced Separation of a Flat-Plate Boundary Layer

When an oblique shock wave impinges upon the surface of a model the pressure rises abruptly through the shock. The pressure gradient produced by the shock is then propagated upstream and downstream of the point of impingement. This leads to a local thickening of the subsonic portion of the boundary layer creating compression waves in the outer flow field. These waves cause additional adjustments in the boundary layer until a final equilibrium state is reached.

If the overall change in pressure is large enough, the boundary layer will separate. The adverse pressure gradient imposed by the outer stream causes fluid within the boundary layer to decelerate forming a region of reversed flow, followed by reattachment. This "bubble" of reversed flow is generally associated with the formation of vortices and large energy losses[2]. In addition, high heating rates are observed near the point of reattachment where the shear layer contacts the surface downstream of the separation bubble.

Because of the detrimental effects of flow separation on vehicle performance, a great deal of effort has been devoted to recognizing separated flows. Surface pressure distributions are often used to identify the "approximate" location and the extent of separation. Three distinct regions can be identified from wall pressure measurements;

(1) an increase in pressure due to separation

(2) a reduced or zero pressure gradient within the separation bubble, and

(3) a pressure rise following reattachment[20].

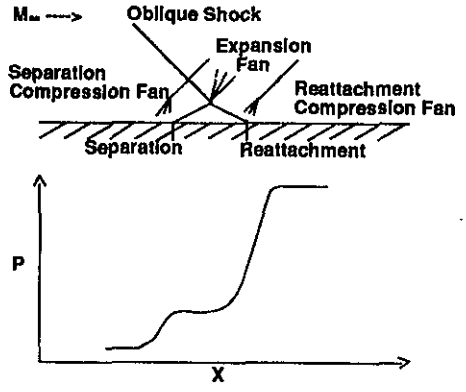

Figure 4 Wall pressure distributions within a separated flow region (from P.R. Viswanath 1988).

A schematic of a typical pressure plot for a shock-induced separation is provided in Figure 4. In addition to surface pressure measurements, schlieren photography and oil flow visualization techniques may be used to determine the approximate separation and reattachment locations.

Static Pressure Measurements

The streamwise pressure distribution, provided in Figure 5, corresponds to a flow deflection angle of 12.5^0. The pressure at the wall (P_W) is normalized by the free-stream static pressure (P_∞), and then plotted against the streamwise distance (X), normalized by the flat-plate length (X_L). The pressure ratio determined from inviscid theory is represented by the horizontal line located to the right of the data.

The static pressure distributions observed are typical of many high-speed shock/boundary-layer interactions [21][22]. Three distinct regions can be identified; (1) an initial pressure rise, (2) a "kink" or an abrupt change in slope, and (3) an increase in pressure to a value slightly greater than that predicted by inviscid theory. The sharp decline in the pressure, which immediately follows the peak pressure, is caused by the trailing-edge expansion fan from the shock generator. The region of interest in the present experiment occurs upstream of the expansion fan.

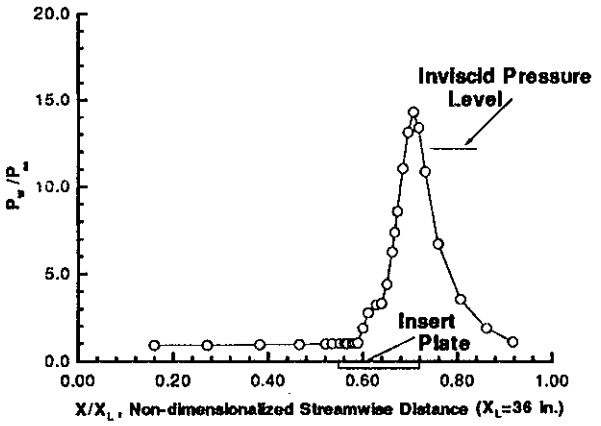

Figure 5 Streamwise surface pressure distribution for the solid surface at a flow deflection angle of 12.5^0.

The discrepancy observed between the inviscid pressure peak and the experimental results can be attributed to several factors. The majority of the experimental pressure rise is due to compression fans introduced by the boundary-layer separation. The flow upstream of the main shock structure passes through a series of compression waves which serve to increase the pressure and entropy of the fluid. In addition, the shape of the oblique shock near the wall and its detachment distance are directly related to the pressure measured at the surface. Since the shock generator has a finite leading-edge thickness, the shock angle is slightly greater than that determined inviscidly.

The spanwise pressure measurements for the $\beta=12.5^0$ test case are shown in Figure 6. The pressure at the wall (P_W) is normalized by the free-stream static pressure (P_∞) and then plotted against the spanwise distance (Y), normalized by the flat-plate width (Y_L). A total of twenty-four pressure orifices, corresponding to three positions downstream of the flat-plate leading edge, are examined. The two static pressure distributions obtained upstream of the oblique shock impingement (X/X_L=0.381, 0.583 inches) are essentially uniform and characteristic of a developing flat-plate boundary layer.

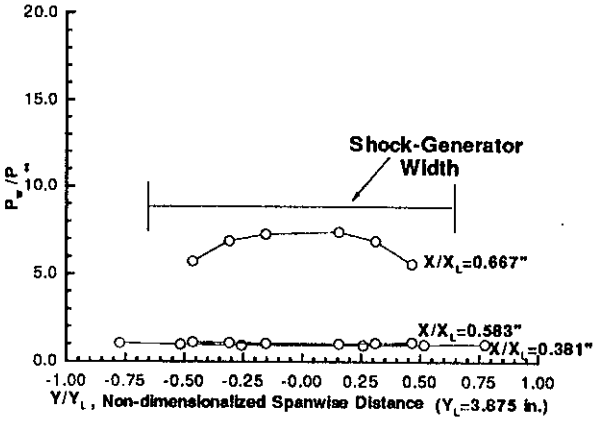

Figure 6 Spanwise surface pressure distribution for the solid surface at a flow deflection angle of 12.5^0.

The spanwise pressures measured immediately downstream of the shock (X/X_L=0.667 inches) are approximately constant at the center, appear curved near the edges $\left(\frac{Y}{Y_t} > \pm 0.25\right)$ of the plot. In the present investigation, one would expect the closest approximation to a 2–D shock/boundary-layer interaction to take

place along the centerline of the model; this is the region which is less likely to encounter end effects produced by the finite-width shock generator mechanism and the tunnel side-wall boundary layer.

Oil Flow Visualization

Oil flow visualization techniques were used to obtain qualitative information about the strength and direction of the surface shear forces. Particular emphasis was placed on determining the extent of two-dimensional flow near the shock impingement location. A light coating of 500cs oil mixed with fluorescent dye was applied to the surface of the flat-plate model. A random covering of small spherical oil drops seemed to work the best. Once the oil flow patterns had developed, the model was illuminated with ultraviolet light and then photographed. Typically regions of high momentum were noted by an absence of oil, whereas regions of separated or reversed flow were noted by an accumulation of oil.

Oil flow visualization results, acquired at a flow deflection angle of 12.5^0, are given in Figure 7. The surface streamline patterns indicate that the flow over the instrumented insert is largely separated. A ridge of oil is formed where the flow upstream of the shock encounters a region of reversed flow (i.e. separation bubble). It is important to note that this "line of accumulation" oscillates upstream and downstream of the actual separation location and is, therefore, only a time-averaged indication of separation. Note that the apparent cellular structure in the oil flow of Figure 7 is not a flow phenomena but is related to the manner in which the oil drops were applied.

Figure 7 illustrates the curved, three-dimensional nature of the shock/boundary-layer interaction. End effects, created by the shock generator mechanism, produce significant regions of 3-D flow near the edges of the instrumented insert plate. Along the centerline of the flat-plate model the flow more closely approximates a two-dimensional interaction. The feasibility of producing a purely two-dimensional shock/boundary-layer interaction has been discussed at length by several authors[23, 24]. Bogdonoff noted that if the shock wave is sufficiently strong or the geometry has a sharp compression corner, "small subsonic regions (will) develop which make it almost impossible to guarantee that the flow is two-dimensional.[24]"

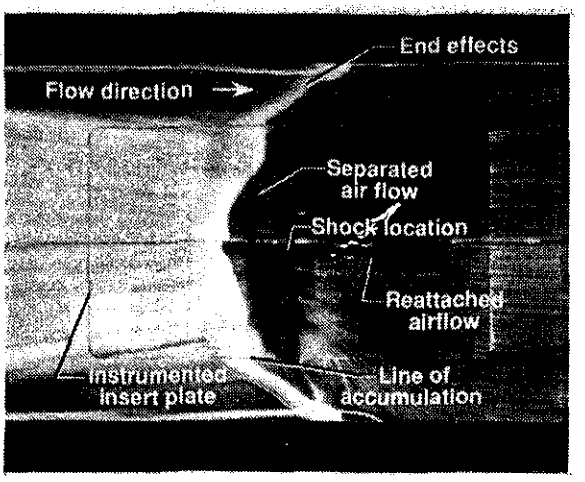

Figure 7 Oil flow visualization of an oblique shock impingement.

Schlieren Photography

Schlieren photographs of the shock/boundary-layer interaction region were obtained for a flow deflection angle of 12.5^0. A photo of the shock generator located opposite the flat plate with the flow directed from left to right is provided in Figure 8. The thin white horizontal line near the bottom of each frame corresponds to the flat-plate boundary-layer edge. The subsonic portion of the boundary layer exhibits local thickening due to the adverse pressure gradient imposed by the oblique shock. This thickening of the boundary layer creates compression waves immediately upstream of the interaction region. A secondary wave formed by the refraction of the incident shock wave is also visible. At the onset of separation, the boundary layer detaches from the surface of the flat-plate model forming a region of reversed flow followed by reattachment. The expansion fan created by the trailing edge of the shock generator mechanism impacts the model surface downstream of this reattachment point. A schematic illustrating the

salient features of a typical shock/boundary-layer interaction was previously shown in Figure 4.

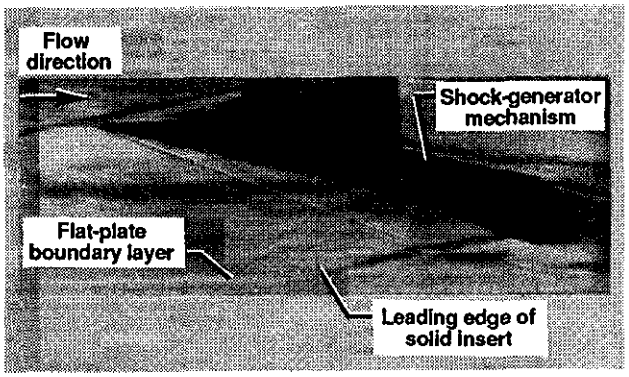

Figure 8 Schlieren photograph of an oblique shock impingement on a solid flat plate.

Porous/Perforated Surfaces

The static pressure distributions for the solid surface are compared to the porous surface measurements at a flow deflection angle of 12.5 degrees. Results from two porous surfaces with porosities of 22% and 28% open are provided in Figure 9. The wall static pressure (P_W) is normalized by the free-stream static pressure (P_∞) and plotted against the non-dimensionalized flat-plate length. The dashed line identifies the solid surface (i.e., 0% porosity) results.

The porous wall pressure distributions, shown in Figure 9, can be divided into three distinct regions: (1) an abrupt pressure rise originating eight to nine boundary-layer thicknesses ($\delta \approx 0.5$ inches) upstream of the baseline pressure increase; (2) followed by a change in the slope of the curve; and (3) an increase in pressure to a peak value measurably less than that observed for the solid surface. The sharp decline in pressure which immediately follows the peak pressure is caused by the trailing-edge expansion fan from the shock generator.

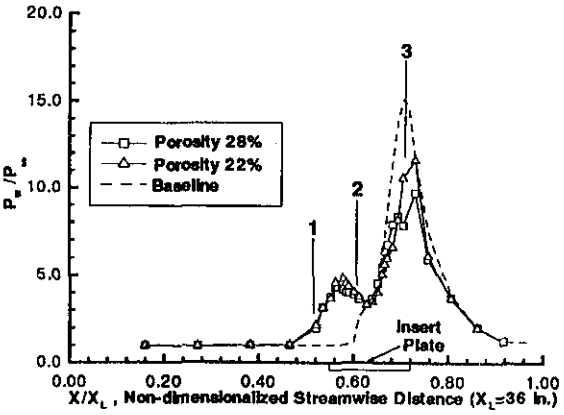

Figure 9 Comparison of porous insert plates at a flow deflection angle of 12.5^0.

Schlieren photography of the flow over a 28% open perforated plate, at a shock-generator angle of 12.5 degrees is provided in Figure 10. The shock-generator mechanism is located opposite the flat-plate with flow directed from left to right. The vertical line located beneath the shock-generator mechanism corresponds to the leading edge of the rectangular cavity. A schematic of the flow field over the perforated insert is sketched in Figure 11.

A comparison of the flow visualization results from Figures 8 and 10, indicates that the presence of surface porosity decreases the strength of the shock wave interaction. As shown in Figure 11, the slower, higher pressure air behind the shock circulates through the rectangular cavity to the low pressure region in front of the shock. This passive "injection" of fluid causes the boundary layer to decelerate and thicken, creating stronger compression waves in the outer flow field than are observed for the baseline case (Figure 8). These waves coalesce forming an oblique shock wave just upstream of the perforated insert, shown in Figure 10. This initial shock wave lowers the Mach number upstream of the externally generated shock wave, thus weakening the strength of the interaction. This result is consistent with the surface pressure distributions, provided in Figure 9, which show a smaller pressure

rise through the external shock wave for the perforated insert.

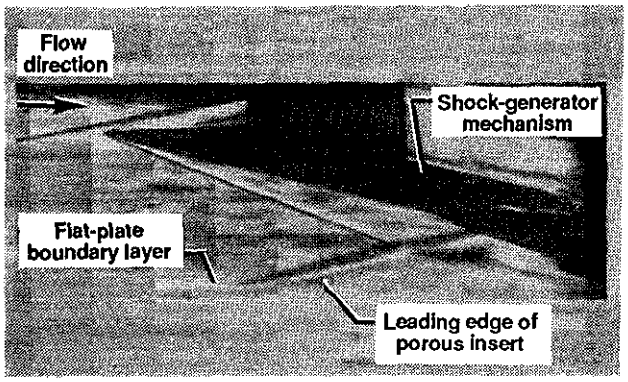

Figure 10 Schlieren Photography of an Controlled Oblique Shock Impingement.

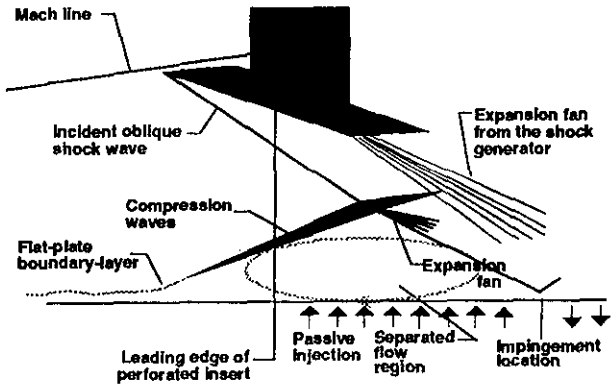

Figure 11 Schematic of shock-wave structure (Porous Wall).

Surface porosity is also observed to extend the length of the interaction region as compared to the baseline (0% porosity) surface. The length of the interaction region is defined as the distance from the initial pressure rise to where the surface pressure distribution sharply decreases due to the shock-generator expansion fan. Figure 9 shows that the initial porous surface pressure rise originates well upstream of the baseline pressure increase. This increase in the interaction length is confirmed by the Schlieren photographs, provided in Figures 8 and 10. The spreading of the interaction region acts to reduce the velocity and pressure gradients through the oblique shock wave. In addition, the heat transfer rates at the base of the shock are most likely reduced. However, further measurements are required to confirm this decrease in the localized heat transfer rate.

The passive "injection" of fluid upstream of the shock impingement separates the boundary-layer, producing a rapid pressure rise. It is important to note that the fluid is "injected" normal to the surface of the flat plate and therefore, reduces the near-wall momentum. Improvements in separation suppression might be achieved by employing streamwise tangential injection.

More detailed measurements, such as boundary-layer surveys downstream of the shock/boundary-layer interaction, are required to properly evaluate the effect of passive control methods on the losses associated with an incident oblique shock wave.

Longitudinal, Transverse, and Swept Grooved Surfaces

The final phase of the experimental investigation examined the effects of surface grooving on the shock/boundary-layer separation. Three groove orientations with respect to the free-stream direction were evaluated; longitudinal, transverse, and swept. The effects of 0.10 inch and 0.05 inch spacings between the grooves were also investigated.

Figures 12-15 compare the baseline (solid surface) and the different grooved surface pressure distributions at a flow deflection angle of 12.5^0. The wall static pressure (P_W) is normalized by the free-stream pressure (P_∞) and plotted

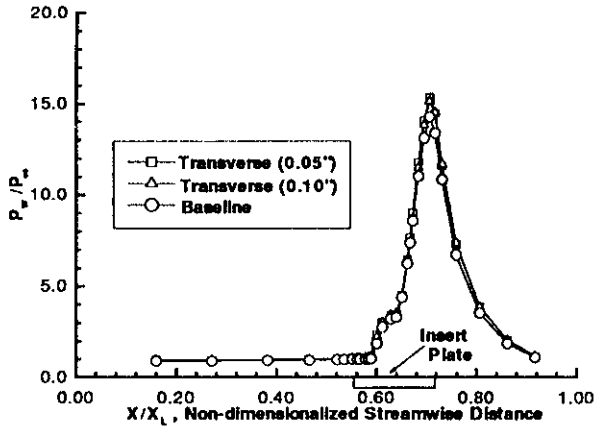

Figure 12 Comparison of Transverse Grooved Insert Plates at a Flow Deflection Angle of 12.5°.

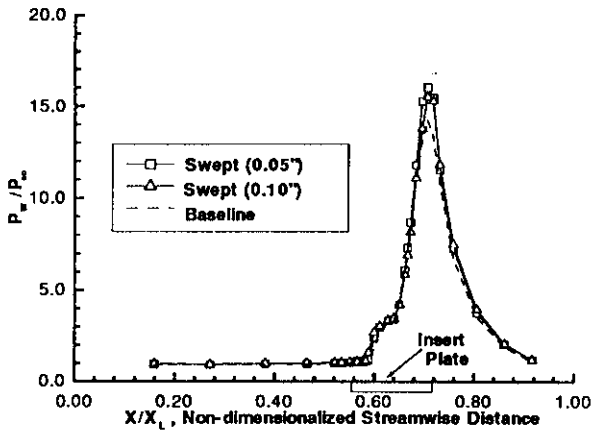

Figure 13 Comparison of swept grooved insert plates at a flow deflection angle of 12.5°.

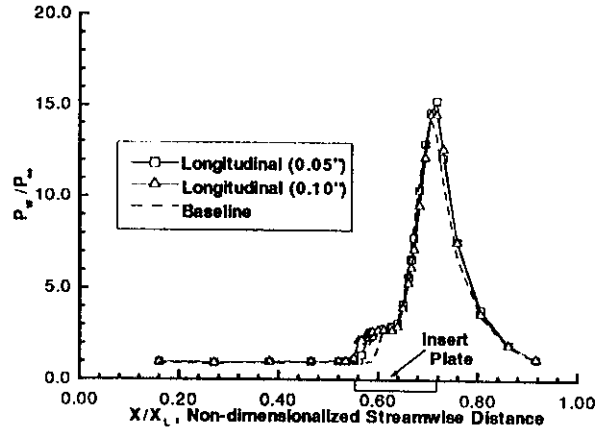

Figure 14 Comparison of longitudinal grooved insert plates at a flow deflection angle of 12.5°.

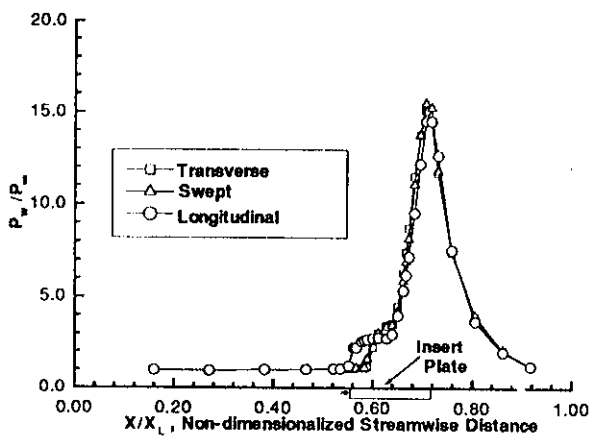

Figure 15 Comparison of grooved insert plates at a flow deflection angle of 12.5°.

against a non-dimensionalized flat-plate length.

Surface pressure distributions for the transverse grooves are provided in Figure 12. The effect of a 0.10 inch (wide) and 0.05 inch (narrow) spacing between the grooves is examined. Initially, the transverse data closely agree with the baseline pressure measurements. Downstream of the shock impingement location, however, the surface pressure rises to a peak value approximately 10% greater than that recorded for the baseline case. The two different groove widths tested have little to no effect on the surface pressure distribution.

Results from the swept groove configurations are presented in Figure 13. The grooves are positioned at alternating sweep angles of -20^0 and $+20^0$, with respect to the free-stream direction. Groove widths of 0.094 inches and 0.047 inches are also examined (see figure 3). The results indicate that the swept grooves, regardless of their width, produce a substantial increase ($\approx$15%) in the pressure value measured near the base of the shock. Once again, the two groove widths have a negligible impact on the surface pressure distribution. This result is consistent with the data acquired for the transverse grooves.

The influence of the longitudinal grooves on the flat-plate static pressure distribution is shown in Figure 14. Groove widths of 0.10 inches and 0.05 inches are evaluated at a flow deflection angle of 12.5^0. The grooved data exhibit an initial pressure rise two to three boundary-layer thicknesses upstream of the reference curve. This pressure increase is qualitatively similar to the porous cavity results observed in the previous section. The longitudinal grooves provide a narrow channel through which fluid downstream of the shock may communicate with fluid upstream of the shock. The grooves act to extend the length of the streamwise interaction region. The peak pressure recorded downstream of the shock-induced separation is slightly lower than that measured for either the transverse and swept grooves, but still higher than that obtained for the reference case. The combination of a higher peak pressure and an increase in the streamwise interaction length suggests that the grooved surfaces decrease the overall performance. Momentum surveys near the interaction region would be required to verify this initial finding.

Research conducted at subsonic speeds indicated that the effectiveness of the grooved surfaces could be attributed to three factors: (1) the grooves shed vorticity which energized the boundary layer, (2) they acted as a laminar boundary layer trip mechanism and (3) they broke up the larger separated region into smaller separated regions performing a function similar to a roller bearing. In the current investigation, the poor performance of the grooved surfaces is related to the absence of two of the three aforementioned separation suppression mechanisms.

The second separation suppression mechanism is not applicable since the flat-plate boundary layer is fully turbulent prior to encountering the grooved surface. The boundary layer transitions from laminar to turbulent flow at the critical Reynolds number of $R_{x_{crit}} = \left(\frac{U_\infty x}{\nu}\right)_{crit} \approx 3.2x10^5$. At the specified wind-tunnel conditions (Re/ft=15.175X10^6) the boundary layer becomes turbulent immediately downstream of the flat-plate leading edge.

For the cavity depth-to-width ratios tested the third mechanism appears to have increased the pressure rise through the oblique shock system. This result is consistent with observations made by Lin[13] which led him to define a critical aspect ratio (a/b) for transition from a closed to an open cavity. Open cavity (a/b>1) flows are characterized by a reattachment at or beyond the rear wall of the cavity. Closed (a/b<1) cavity flows are characterized by a reattachment along the floor of the cavity and an increase in the viscous losses. All of the grooved surfaces investigated had an aspect ratio of 1.0, better results might have been achieved if this aspect ratio were increased.

Computational Results

Shock-Induced Separation of a Flat-Plate Boundary Layer

Comparisons were made between the computed solutions and the experimental results for a shock-generator angle of 12.5^0. The angle selected was of sufficient strength to produce large regions of separated

flow. The nominal test conditions for this investigation were $M\infty=6.0$, T_w=adiabatic, and $Re=15x10^6$ per foot. The algebraic turbulence model, proposed by Baldwin and Lomax[19], was used to close the system of equations.

Features of this high-speed, compressible flow were investigated using the computational grid depicted in Figure 16. The 2–D, rectangular grid has a mesh density of 100x150. Adequate resolution of the viscous interactions required that the grid be refined near the surface of the flat plate. Therefore, the grid points were clustered in the normal (z) direction, while the grid spacing in the tangential (x) direction remained uniform.

Computational results from a grid refinement study are presented in figure 17. Surface pressure distributions acquired in the Mach 6 High Reynolds Number Tunnel are compared to the computed results for three different mesh densities (34x81, 51x81, and 100x150). The pressure at the wall (P_W) is normalized by the free-stream static pressure (P_∞), and then plotted against a non-dimensionalized reference length (X/X_L). The initial grid density is far too coarse to sufficiently resolve the experimentally observed pressure rise. The second and third mesh densities more closely agree with the experimental data, except near the separation region.

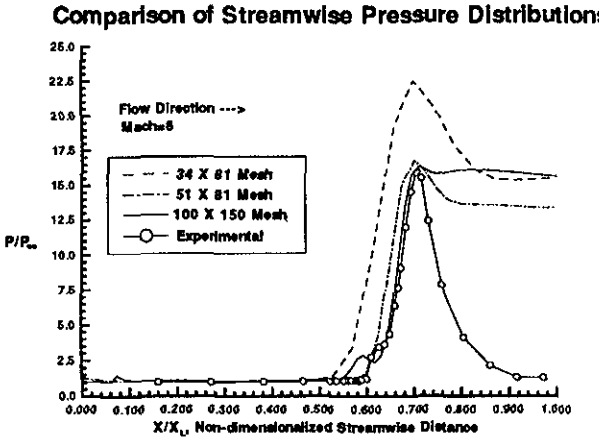

Figure 16 Comparison of computational and experimental wall pressure distributions.

Conclusions & Recommendations

An investigation into the effect of passive control methods at high speeds and high Reynolds numbers has been conducted. The following conclusions may be drawn from the experimental and computational data:

(1) Porous surface inserts noticeably diminished the pressure gradients in the interaction region. The surface with the highest porosity produced the greatest reduction in the pressure rise measured through the shock.

(2) Schlieren photography showed that porous surface mass transfer produced compression waves which served to weaken the primary shock system.

(3) Porous surfaces were found to decrease the peak pressure, but extend the length of the separated region in the streamwise direction.

(4) Although the grooved insert plates have proven effective at lower speeds in other investigations, they had an unfavorable effect on the shock-induced separation of a hypersonic boundary layer. Significant increases in the peak pressure were observed for each of the different groove orientations and groove spacings.

(5) Computational results from a two-dimensional Navier-Stokes code were found to be in good agreement with the experimental data. Closer agreement between the two solutions might be achieved by extending the solution to three-dimensions and/or employing a turbulence model more suited to highly separated flows.

The next logical step would be to computationally model the turbulent flow over a two dimensional rectangular cavity with surface porosity. The results from these computations should provide valuable information about the physics of the flow. In addition, a parametric study should be conducted to address the influence of several factors including the degree of surface porosity, and the location of the rectangular cavity.

It is also suggested that more detailed measurements be acquired to access the viscous losses associated with the shock/boundary-layer interaction.

Acknowledgments

Special thanks to Chris Rumsey, Ralph Watson and Leon Morrisette from NASA LaRC for their input during several thought-provoking discussions.

References

[1] S. M. Bogdonoff and K. Poddar. An exploratory study of a three-dimensional shock wave turbulent boundary-layer interaction in a corner. *AIAA 91-0525*, January 1991.

[2] H. Schlichting. *Boundary-Layer Theory*. McGraw-Hill Book Company, Copyright 1979.

[3] P. Krogmann. *Transonic Drag Reduction By Active/Passive Boundary Layer Control*. VKI Lectures.

[4] A. Bertelrud. Shock-boundary layer interaction in flight. *NASA Transonic Symposium*, 1988.

[5] J. Delery. Shock-wave/turbulent boundary-layer interaction and its control. *Prog. Aerospace Sci., Vol. 22*, 1988.

[6] H.T. Nagamatsu; T.W. Trilling; and J.A. Bossard. Passive drag reduction on a complete NACA 0012 airfoil at transonic Mach numbers. *AIAA 87-1263*, 1987.

[7] S. Bauer and G. Hernandez. Reduction of cross-flow shock-induced separation with a porous cavity at supersonic speeds. *AIAA 88-2567*, 1988.

[8] H.W. Liepmann and A. Roshko. *Elements of Gasdynamics*. John Wiley & Sons, Inc., New York, 1957.

[9] V.K. Migay. The efficiency of a cross-ribbed curvilinear diffuser. *Energomashimostroyeniye, No. 1, pp. 45–46*, 1962.

[10] V.K. Migay. A study of finned diffusers. *Teploenergetika, No. 10, pp. 55–59*, 1962.

[11] F.G. Howard; B.F. Quass; L.M. Weinstein; and D.M. Bushnell. Longitudinal afterbody grooves and shoulder radiusing for low-speed bluff body drag reduction. *ASME 81-WA/FE-5*, 1990.

[12] F.G. Howard; W.L. Goodman; and M.J. Walsh. Axisymmetric bluff-body drag reduction using circumferential grooves. *AIAA Applied Aerodynamics Conference*, July 13-15, 1983.

[13] J.C. Lin; F.G. Howard; and D.M. Bushnell. Investigation of several passive and active methods for turbulent flow separation control. *AIAA 90-1598*, 1990.

[14] R.A. Jones and V.F. Williams. Preliminary surveys of the wall boundary layer in a Mach 6 axisymmetric tunnel. *NASA TN D-562*, 1970.

[15] V.N. Vatsa and J.L. Thomas. Computations of prolate spheroids at angle of attack. *AIAA 87-2627CP*, 1987.

[16] R. Beam and R.F. Warming. An implicit finite difference algorithm for hyperbolic systems in conservation-law-form. *Journal of Computational Physics, Vol. 22*, September 1976.

[17] P.L. Roe. Characteristic-based schemes for the Euler equations. *Annual Review of Fluid Mechanics, Vol. 18, pp. 337-365*, 1986.

[18] T. Cebeci and A.M.O. Smith. *Analysis of Turbulent Boundary-Layers*. Academic, New York, 1974.

[19] B.S. Baldwin and H. Lomax. Thin layer approximation and algebraic model for separated turbulent flows. *AIAA 78-257*, 1978.

[20] P.R. Viswanath. Shock-wave-turbulent-boundary-layer interaction and its control: A survey of recent developments. *Sadhana, Vol. 12, Parts 1 & 2, pp. 45–104*, February, 1988.

[21] C.B. Johnson and L.G. Kaufman II. Interference heating from interactions of shock waves with turbulent boundary layers at Mach 6. Technical report, NASA Technical Note D-7649, 1974.

[22] G.S. Settles; I.E. Vas; and S.M. Bogdonoff. Details of a shock-separated turbulent boundary

layer at a compression corner. *AIAA Journal, Vol. 14, No. 12*, Dec. 1976.

[23] G.S. Settles; S.M. Bogdonoff; and I.E. Vas. Incipient separation of a supersonic turbulent boundary layer at high Reynolds numbers. *AIAA Journal, Vol. 14, No. 1*, 1975.

[24] S.M. Bogdonoff. The modeling of a three-dimensional shock wave turbulent boundary layer interaction. *AIAA 90–0766*, 1990.